Delamination of 2D coordination polymers: the role of solvent and ultrasounds

N. Contreras-Pereda[a], P. Hayati[a], S. Suárez-García[a], L. Esrafili [c], P. Retailleau[d], S. Benmansour[e], F. Novio[a], A. Morsali*[c] and D. Ruiz-Molina*[a]

[a]Catalan Institute of Nanoscience and Nanotechnology (ICN2), CSIC and BIST, Campus UAB, Bellaterra, 08193 Barcelona, Spain E-mail: dani.ruiz@icn2.cat

[b]Young Researchers and Elite Club, Dashtestan Branch, Islamic Azad University, Borazjan, Iran

[c]Department of Chemistry, Institution: Faculty of Sciences, Tarbiat Modares University, 14115-175, Tehran, Iran

[d]Institut de Chimie des Substances Naturelles, CNRS UPR 2301, Univ. Paris-Sud, Université Paris-Saclay, 1, av. de la Terrasse, 91198 Gif-sur-Yvette, France

[e]Instituto de Ciencia Molecular, Parque Científico. Universidad de Valencia. José Beltrán 2, 46980 Paterna (Valencia) Spain

Abstract: Two novel cadmium-based 2D coordination polymers have been synthesized and characterized. Experimental results evidence that the best delamination processes occurs when weak interactions dominate the cohesion between layers, modulated by solvent molecules occluded within the crystalline network. In this case, the delamination of the crystals occurs spontaneously in water whereas nanoflakes though they can also be obtained by ultrasound-assisted liquid phase exfoliation in solvents such as ethanol or acetone. However, when interlayer solvent molecules are coordinated to metal centers, more robust structures are obtained, making very difficult the delamination process. This study shows how the physicochemical properties and structure of the bulk crystals determine the success of the exfoliation process in which the sonication method and type of solvent used are critical parameters. These systems offer also platform to study different experimental parameters and approaches (ultrasound bath vs. probe tip) on the delamination of these 2D materials.

Keywords: 2D-structures, coordination polymers, nanomaterials, delamination process, ultrasound-assisted process

Introduction

Single- or few-layers exfoliated 2D materials exhibit original properties in comparison with bulk counterparts, offering innovative routes to explore fundamental phenomena at the nanoscale while enabling novel applications [1,2]. Several different 2D materials have been so far described, among them graphene or transition metal dichalcogenides showing unique outcomes [3]. However, and in spite of the exponential growing number of scientific works devoted to the area, the design of 2D materials with fine-tuned properties still remains a challenge. Recently, coordination polymers (CPs) have emerged as novel versatile materials with interesting tunable properties based on the quasi infinite number of combinations between metal centers and polydentate ligands. In addition to its rich chemical flexibility, 2D-CPs contain metallic ions that confer novel optical, magnetic and/or electrical properties [4]. All these premises have already crystallized in different examples of 2D materials relevant for the electrochemical detection of H_2O_2 [5], functional thin films [6], molecular sieve membranes [7], polymer composites for gas separation [8-9], catalysis [10-11], photoluminescence [12-13], or several electronic applications [14] such as field effect transistors [15], chemoresistive gas sensors [16] including e-textiles [17], electrochemical oxygen reduction catalysts [18], supercapacitors [19-21] or spin-cross over systems [22].

2D-CPs can be obtained using bottom-up approaches [23-25] such as the liquid-liquid interface synthesis [26-28]. With this approach, sheets with large aspect ratios and nanometer thickness have been reported, although as a main disadvantage the procedure requires outsized reaction times [26]. To avoid this limitation, some authors have developed new methodologies to induce a fast diffusion of the reactants by increasing the temperature reaction, leading though to the uncontrolled synthesis of nanocrystals coexisting with bulk materials and platelets [26]. Other procedures based on surfactant-assisted solvothermal synthesis may also allow for control over the reaction. Nevertheless, the removal of the surfactant excess is problematic [29-32], requiring of additional annealing [30] or reflux in ethanol or chloroform [32].

A successful alternative is the so-called liquid phase exfoliation (LPE) process, consisting in the top-down delamination of bulk crystals [33-36]. This can be achieved by submerging the crystals in a solvent, without any additional source of energy. For instance, Zamora et al. reported the delamination of $[Cu(\mu\text{-}pym_2S_2)(\mu\text{-}Cl)]_n$ compound crystals into nanosheets (1.5

nm - 2.5 nm thick) simply by immersion in water [37]. However, in most of the cases a solvent-assisted sonication [38] is required to obtain the delaminated material [39]. For this reason, further basic studies that allow us to understand and therefore to control the role of sonication on the delamination of 2D materials is highly required.

Beyond the nature of the solvent used, the delamination process can be also fine-tuned with the intercalation of specific chemical groups between the 2D-layers that modulate the interaction between layers and their subsequent exfoliation [40-42]. For instance, Cheetham et al. proved the liquid exfoliation in different solvents of isostructural Cu and Zn complexes incorporating weakly interacting chains [33] and Banerjee et al reported the synthesis of three isostructural metal-organic polyhedra exposed to different alkyloxy chains in their outer surface [43]. Alternatively, Vittal et al. pointed out to the relevance of intercalated solvent molecules in the delamination process reporting five 3D bulk lanthanide isostructural complexes with DMF solvent molecules entrapped [44]. After soaking into dimethylacetamide (DMA), solvent exchange takes place in all five structures, resulting in 40-100 nm nanoplates that retain the bulk properties. In spite of these pioneering results, the role of crystallization solvent molecules in the delamination process is not fully understood in spite of its relevance.

In this work a systematic study of two related cadmium-based 2D-CPs, where the interstitial solvent plays a differential role, is reported. On one hand, in complex $[Cd(oba)(bpfb)]_n \cdot xDMF$ (**1**), where oba means 4,4'-oxybis(benzoic acid) and bpfb μ-N,N'-bis(4-pyridyl formamide)-1,4-benzene, the solvent molecules occupy interstitial voids between weakly interacting layers mainly by Van der Waals interactions. On the other hand, complex $[Cd(5\text{-aip})(DMF)_2]_n$ (**2**), where 5-aip means 5-aminoisophthalic acid, presents DMF as solvent molecules directly coordinated to metal centers acting as an effective linker between layers. A schematic representation of both structures together with an illustration of the ultrasound assisted process followed is shown in Figure 1. Whereas the delamination of complex **1** has been achieved under very mild conditions, the structure of complex **2** is notably stabilized, interfering in the proper delamination of the flakes. To assess such influence, different sonication methods have been applied on the quest for the optimal delamination. In all the cases, water seems to be the more efficient soamination of complex **1** though it exhibits a clear time dependent sonication exfoliation in other solvents.

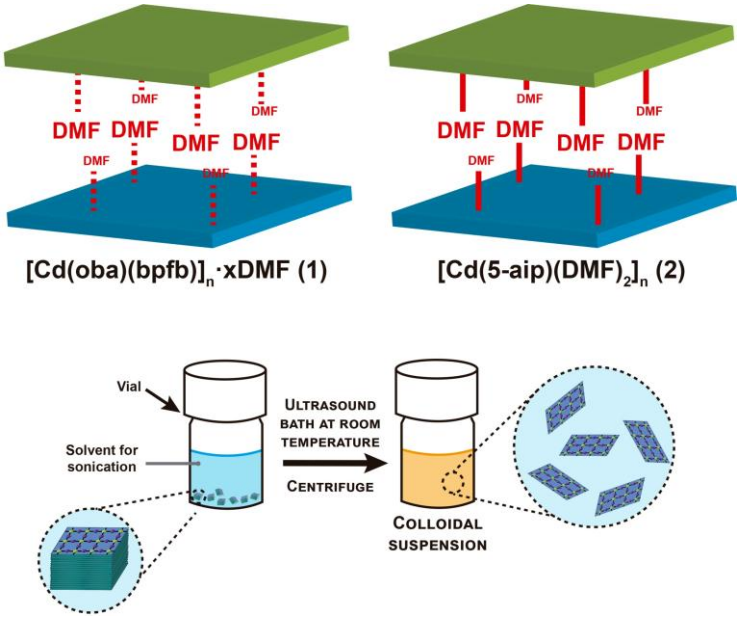

Figure 1. (Top) Schematic representation of the different configuration of DMF solvent molecules in layered complexes **1** and **2**. (Bottom) Representation of the ultrasound assisted LPE process followed for the delamination of complexes **1** and **2**.

Results and Discussion

Synthesis and characterization of complexes 1 and 2

*Synthesis and characterization of complex **1**.*

Reaction between cadmium (II) nitrate, and a mixture of 4,4'-oxybis(benzoic acid) (oba) and μ-N,N'-bis(4-pyridyl formamide)-1,4-benzene (bpfb) in DMF yielded a crystalline material formulated as $[Cd(oba)(bpfb)]_n \cdot xDMF$ (**1**). Suitable crystals for X-Ray diffraction were obtained and its structure shown in Figure 2. Complex **1** crystallizes in the triclinic $P\bar{1}$ space group as a 2D supramolecular coordination network (crystallographic details are given in Supporting Information, Table S1), where pyridyl groups of bpfb coordinate Cd(II) ions in axial positions and the equatorial plane is occupied by the oba ligands which coordinate Cd(II) ions through carboxylic groups (see Figure 2a). Each Cd(II) ion is coordinated to two oba ligands which bridge the metal ion with other adjacent Cd(II) ion forming Cd(II) dimers, and other oba ligand that coordinates Cd(II) in a chelate mode and interconnects adjacent Cd-Cd dimers.

As a result, one of the carboxylic groups from oba ligands act as chelate ligand to one of the Cd centers and the other carboxylic group act as a bridge between Cd centres in the equatorial positions. Thus Cd dimers are formed by two metal centers interconenced by carboxyl bridges of different oba ligands, and adjacent dimers are connected by oba ligands. The two remaining coordination positions are occupied by bpfb ligands that interconnect Cd centers in the axial position. This structural arrangement results in the formation of 2D layers that consist on double rows of bpfb-Cd dimers units connected by oba ligands that appears in a zigzag configuration (see Figures 2b-c). The structural stabilization of the double rows is due to the supramolecular π-π stacking interactions between the aromatic rings of bpfb ligands.

Regarding the 2D layers, they pack along the (1-21) plane with an interlayer distance of 6.106 Å. Globally, C……H and O……H intermolecular interactions are most abundant in the crystal packing (21.7%, and 19.5%, respectively according to Hirshfeld surface analysis). It is evident that van der Waals forces and hydrogen bonds exert an important influence on the stabilization of the packing in the crystal structure, and other interlayer interactions [H……H (4.4%), O…...O (5%) and Cd……H (0.4%)] contribute less. The structure formed leads to the generation of cavities between the layers of the crystal allowing the location of DMF solvent molecules (Figure 2d). Moreover, the formation of stabilizing N−H……O hydrogen bonds takes place in two ways: in the interlayer and between DMF molecules and layers with a bonding distance of 2.352 Å and 1.981 Å, respectively. Thus, DMF molecules are linked to the 2D layers through labile hydrogen bonds.

The coordination of complex **1** was corroborated by FT-IR (see Supporting information, Figure S1). The band at 3330 cm^{-1} attributed to the pyridine ring present in bpfb ligand is shifted to higher frequency (~3370 cm^{-1}) and its intensity strongly suppressed due to the deformation of the ring after the coordination with Cd(II) ions. On the other hand, the coordination of the carboxylic groups to Cd(II) ions, is confirmed by the presence of the characteristic bands of the COO^- at v = 1594 cm^{-1} and v = 1385 cm^{-1}. The prevalence of carboxylic groups from oba ligands is observed by the presence of characteristic vibrational bands of C=O and C−OH in the range of 1680−1580 cm−1 and 1250−1200 cm^{-1}, respectively. Additionally, typical bands from bpfb (v = 1320, 829, 662) and oba (v = 1592, 1248, 773) ligands are observed in the IR spectra.

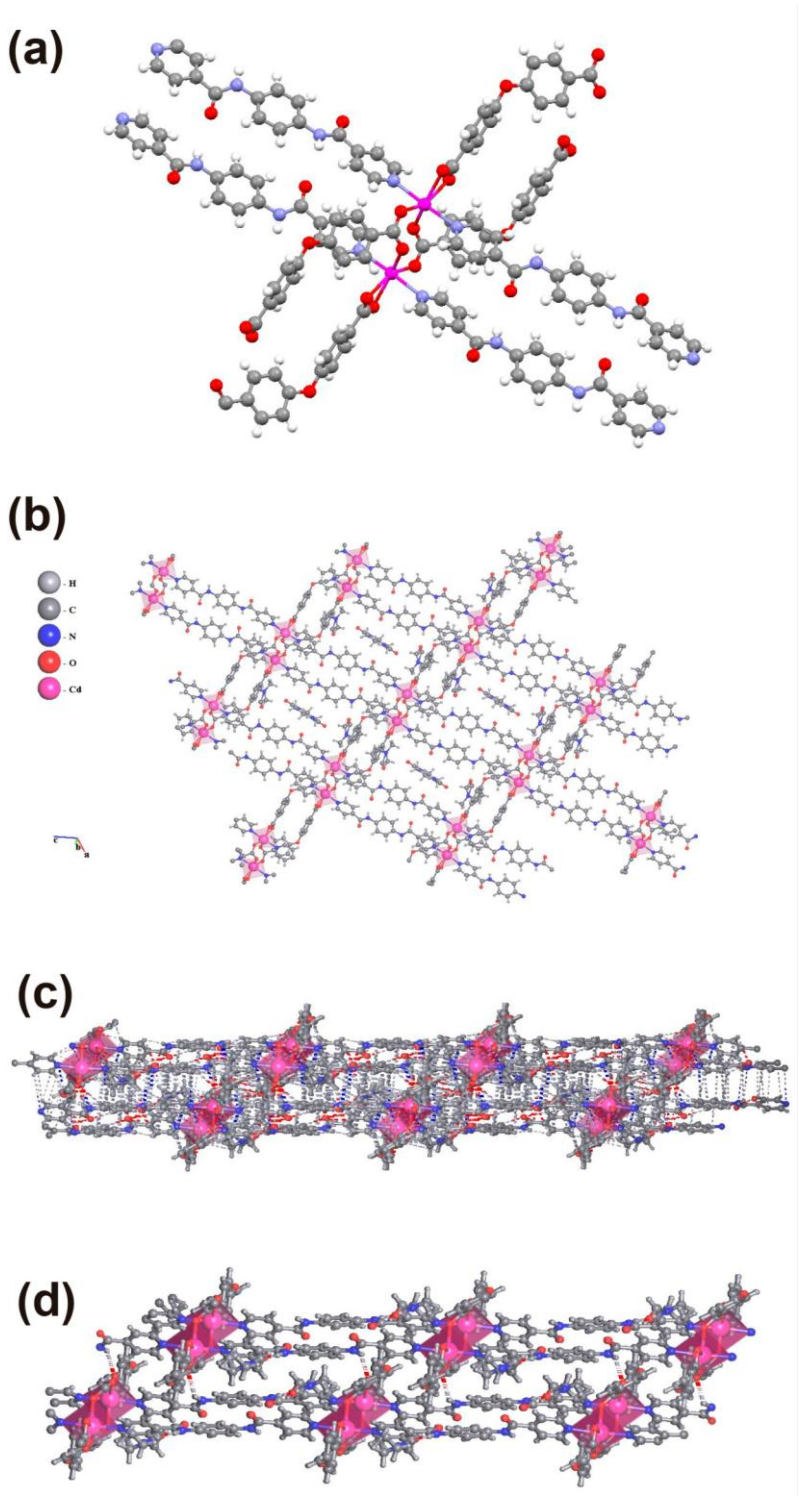

Figure 2: (a) Coordination surrounding of the Cd dimers in complex **1** (b) Top view of on layer structure of complex **1** (c) Side view of two layers showing the supramolecular Van der Waals interactions between them (d) Side view of two layers showing the supramolecular hydrogen bonds between them and with DMF molecules.

*Synthesis and characterization of complex **2**.*

Reaction between 5-aminoisophthalic acid (5-aip), and cadmium (II) nitrate in DMF yielded a crystalline material formulated as $[Cd(5\text{-aip})(DMF)_2]_n$ (**2**). Single crystals suitable for X-ray diffraction analysis were obtained by the slow diffusion method. Complex **2** crystallizes in the monoclinic *C*2/*c* space group as a 2D supramolecular coordination network (crystallographic details are given in Supporting Information, Table S1), where 5-aip ligands coordinate Cd(II) ions by their carboxylic terminations in the equatorial positions of the coordination sphere (see Figure 3). Each Cd(II) ion is coordinated to one 5-aip ligand in a chelate mode and two 5-aip ligands that bridge the metal ion with other adjacent Cd(II) ion forming in this way Cd(II) dimers. The axial positions of the metal ions are occupied by DMF molecules. According, to the solved structure, layers pack along the plane (100) and the interlayer distance is 8.021 Å. As a result, complex **2** is expanded in a 2D-layer and the presence of coordinated DMF molecules in the interlayer space determines the weak interaction between 2D layers.

Globally, C……O and O……H intermolecular interactions are most abundant in the crystal packing (21.7%, and 55%, respectively according to Hirshfeld surface analysis). The layers are connected mainly by weak van der Waals interactions, having an important influence on the stabilization of the packing in the crystal structure. Other interactions as H……H (6.6%), O…..O (4.8%) and Cd……O (0.8%) contribute less. As seen in Figure 3d, the coordinated DMF molecules from adjacent layers interact between them and with the adjacent layer only by means of van der Waals interactions. The FT-IR spectrum (see Supporting Information, Figure S2) shows the vibrational bands characteristic for the coordination between the carboxylic groups from 5-aip (C=O and C−OH in the range of 1680−1580 cm^{-1} and 1250−1200 cm^{-1}, respectively) and Cd(II) ions which are shifted with respect to the initial free ligand spectrum due to its coordination. Furthermore, a shift was also observed in the characteristic band of the carbonyl group around 1390 cm^{-1}.

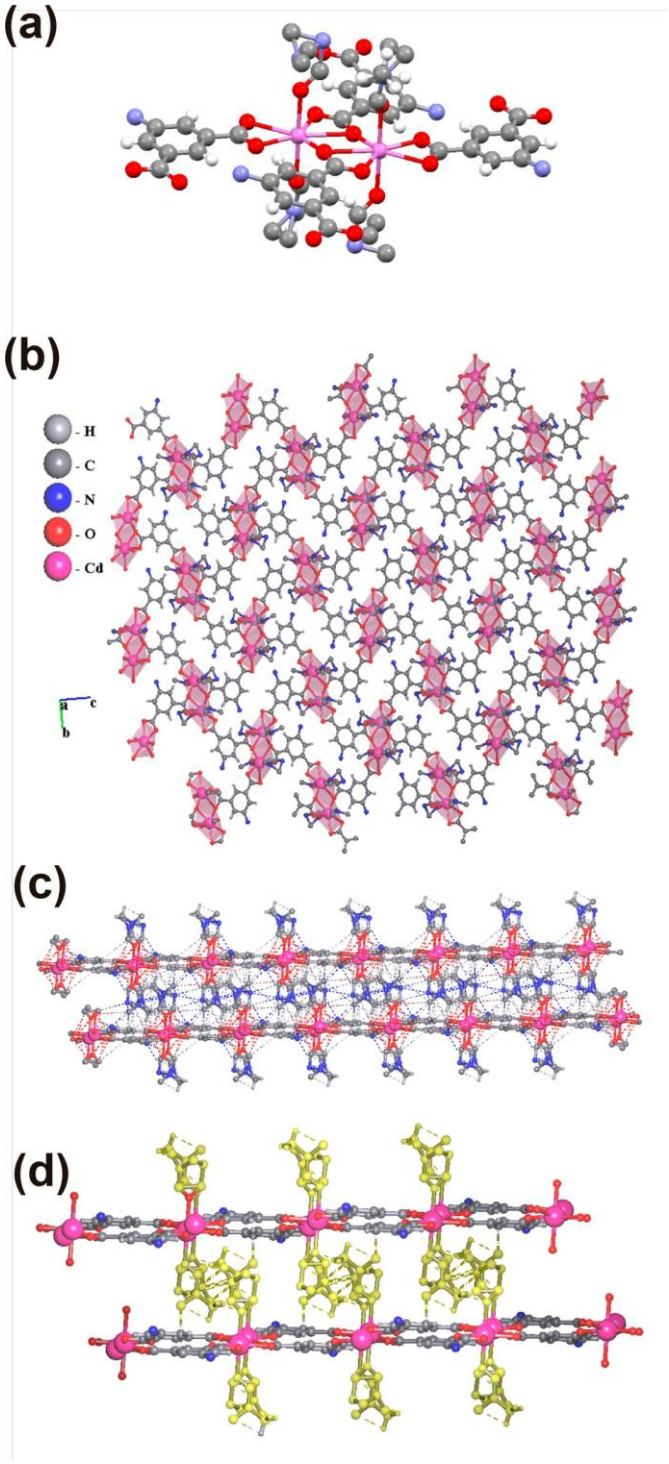

Figure 3: (a) Coordination surrounding the Cd dimers in complex **2** (b) Top view of one layer of complex **2** (c) Side view of two layers showing the interlayer supramolecular van der Waals (d) Side view of two layers showing the supramolecular van der Waals bonds between them and with highlighted DMF molecules.

Solvent-induced delamination of complexes 1 **and** 2

Crystals of complex **1** were manually selected, washed with DMF and dried (see Supporting Information, Figure S3). The XRPD powder spectrum of the resulting crystals exhibited less intense peaks and a different pattern than the as-synthesized material. Interestingly, the crystallinity and original phase can be fully recovered upon submerging the crystals (2 mg/mL) back in DMF for a few hours (see Supporting Information, Figure S4) indicating a reversible desolvation-solvation process and the lability of intercalated solvent molecules. Moreover FT-IR spectra corroborated the chemical stability of the complex along the drying-wetting process (see Supporting Information, Figure S5). Interestingly, if the dried crystals are dipped in water, the crystallinity of the sample is increased resulting though in a novel crystalline structure, which turns out to be more stable than the one with DMF, as corroborated after re-dispersion of the crystals in DMF. Finally, in ethanol and acetone the pattern of the dried crystals is retained (see Supporting Information, Figure S6), indicating no significant effect of the solvent.
This fact aims us to study the immersion of the crystals in all four solvents for longer periods of time (lower concentrations were used for these experiments, 0.25 mg/mL). Representative scanning electron microscopy (SEM) images of the self-exfoliated films in water after one day and one month of immersion are shown in Figure 4. As observed there, sub-micrometer thick films organized in star-like morphologies after drying are obtained within the first day. A statistical analysis of the films thicknesses obtained from several different samples (see Supporting Information Figure S7) shows a rather broad distribution centered at a mean thickness size of 478 ± 255 nm. Similar films (mean size of 454 ± 222 nm) are obtained after one month of immersion (see Supporting Information Figure S8).
No significant delamination of complex **1** was detected over a month in any of the other three solvents (DMF, ethanol and acetone). Similar results were found for complex **2** (see Supporting information Figures S9 and S10), which did not show any delamination process not even in water, reason why additional experiments under sonication were now repeated.

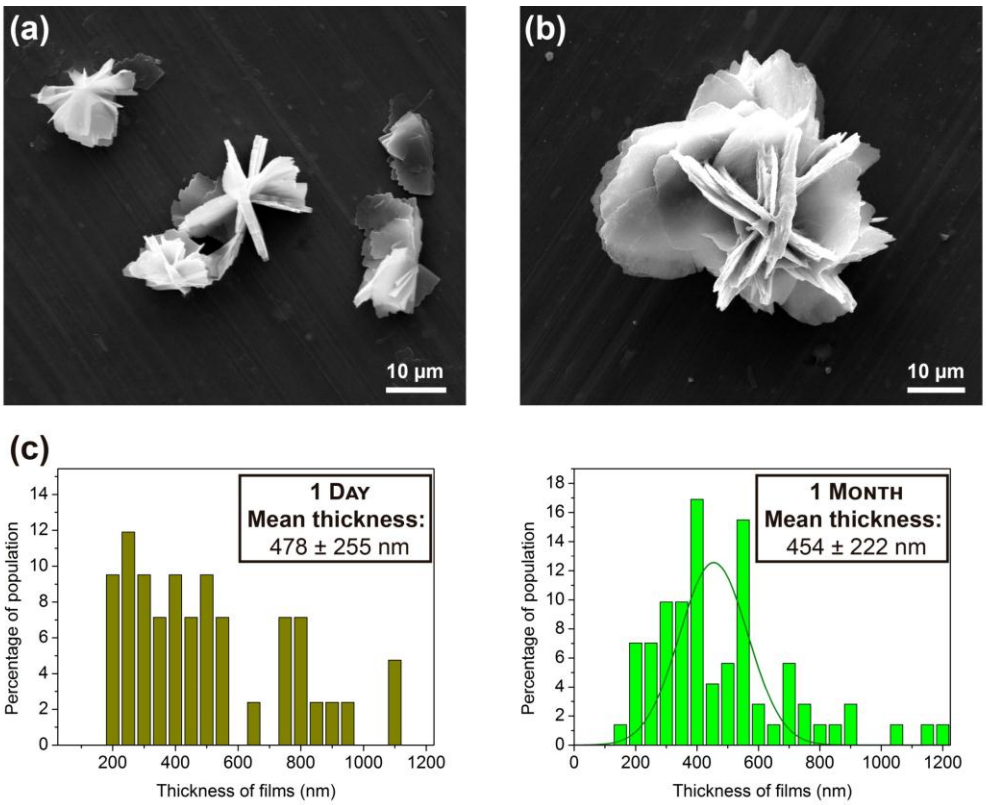

Figure 4. SEM images of the colloidal suspensions of **1** obtained after (a) one day and (b) one month of the immersion of the crystals in water. (c) Size distribution statistics of the thicknesses of films obtained after one day (left) and one month (right) of immersion of **1** in water.

Ultrasounds-assisted delamination of complexes 1 **and** 2

Bath assisted sonication. First attempts to delaminate complex **1** in DMF assisted with an ultrasound bath were unsuccessful in spite of the different experiments tested. In all the cases fragmentation in smaller crystals with less defined morphologies were found from where only a small fraction of flakes was identified (see Supporting Information, Figure S11). Afterwards, the delamination process was tested in ethanol, acetone and water at different sonication times of 4, 6 and 8 hours. In all cases the exfoliation takes place with a defined tendency to increase the delamination yield with sonication time, reaching a maximum at 8h (see Supporting Information, Figure S12). After this time, centrifugation allows for the removal of the non-exfoliated material, which deposits at the bottom of the centrifugation tube, meanwhile the exfoliated flakes remain as a stable colloidal suspension that can be recovered and isolated.

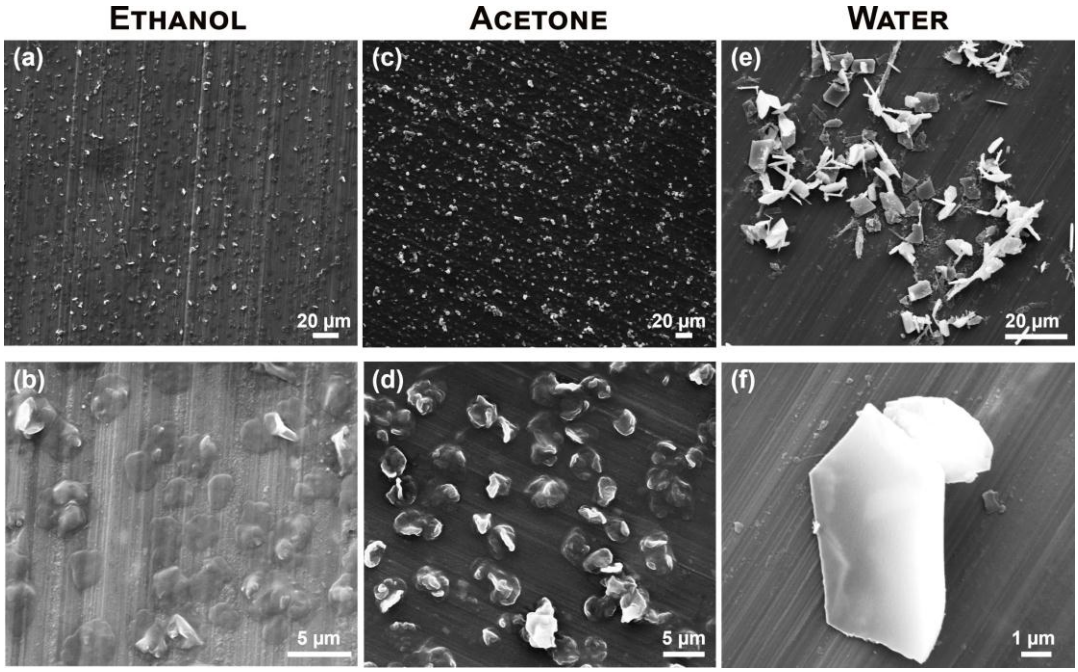

Figure 5. SEM images of the colloidal suspensions of complex **1** obtained after optimization of the sonication time with the ultrasound bath and centrifugation (1 min, 7000 rpm) in (a-b) ethanol, (c-d) acetone and (e-f) water. Images (b), (d) and (f) are a large magnification image of the samples imaged in (a), (c) and (e) respectively. Images (a-d) prove the obtaining of flakes with lateral sizes of the order of 1-2 µm in ethanol and acetone. On the other hand, images (e-f) show the exfoliation of **1** into nanometre-thin films with lateral sizes of the order of 5 µm.

Dynamic light scattering (DLS) measurements of the colloidal dispersions obtained in ethanol and water show a good monodispersion with average dimensions of 280 nm and 290 nm, respectively (see Supporting Information, Figure S13). DLS measurements repeated five days later, provide very similar size distributions confirming the stability of the colloidal dispersion (Figure S14). However, aggregation-disaggregation processes were detected in acetone as evidenced by the variation of the average sizes found along the measurements even at short periods of time. SEM images of the resulting flakes after 8 hours of ultrasonication in all three solvents are shown in Figure 5. Delamination in ethanol and acetone results in relatively monodispersed films with average diameters of 2-3 µm (Figure 5a to 5d). The exfoliated material in water is obtained as thin flat-shape hexagonal film with large lateral sizes close to 5 µm (Figure 5f).

Different attempts to achieve the exfoliation of **2** in DMF, ethanol and water using the ultrasound bath for 8 h result in the fragmentation of the crystals instead of the desired

delamination process (see Supporting Information, Figure S15). Only in the case of acetone partial formation of flakes could be detected tough in low amounts and always mixed with smashed crystals, making difficult their manipulation and isolation (see Supporting Information, Figure S16). The few observed flakes present a rather irregular shape with lateral sizes of 5 µm. Shorter sonication times lead to large amounts of non-exfoliated bulk materials. On the other hand, larger periods afford further breaking of the crystals.

Tip assisted sonication. Same experiments were repeated by sonicating now with a tip at three different times of 20, 40 and 80 minutes. As the previous results showed that delamination of **1** in DMF was unsuccessful, the exfoliation process was directly performed with ethanol, acetone and water. Representative images of the materials obtained at each sonication time for the three solvents can be found in Supporting Information (Figure S17). Once more, best results are obtained for the longest sonication times (80 minutes). Figure 6 shows representative images of the films obtained with the probe tip (80 minutes) after centrifugation of the surplus non-exfoliated material. As seen there, the delamination in ethanol and acetone provides films 2-3 µm long similar to those obtained with the ultrasounds bath (Figures 6a to 6d). Shorter sonication times lead to a high amount of non-exfoliated material, resulting in a low exfoliation yield. Worth to mention, the resulting colloidal dispersions also show in all the cases a low reproducibility and non-consistent DLS measurements, by comparison with those obtained with the ultrasound bath (see Supporting Information, Figure 18).

For comparison purposes, Figure 7 shows representative cross section images of the flakes obtained in water with the ultrasound bath and probe tip methods. Statistic measurements over a large number of films show mean sizes of 218 ± 73 and 115 ± 33 nm for the bath and tip, respectively with a relatively good monodispersion (see Supporting Information, Figures S19-S20). The chemical stability was also confirmed by FT-IR spectroscopy, upon comparison of the spectra associated to the initial crystalline material and the flakes (Figure S21). Only a small blue shift can be noticed for the peaks corresponding to the carboxylic groups (vC=O, ~ 1650 cm^{-1}) and the C-N bond (~1245 cm^{-1}). This increase in energy is characteristic of the reduced and nanometer thicknesses of the films [45]. Additional FT-IR measurements after ten days indicate no variation of the initial spectrum corroborating the high chemical stability of the exfoliated material over long periods of time in water (see Supporting Information, Figure S21b).

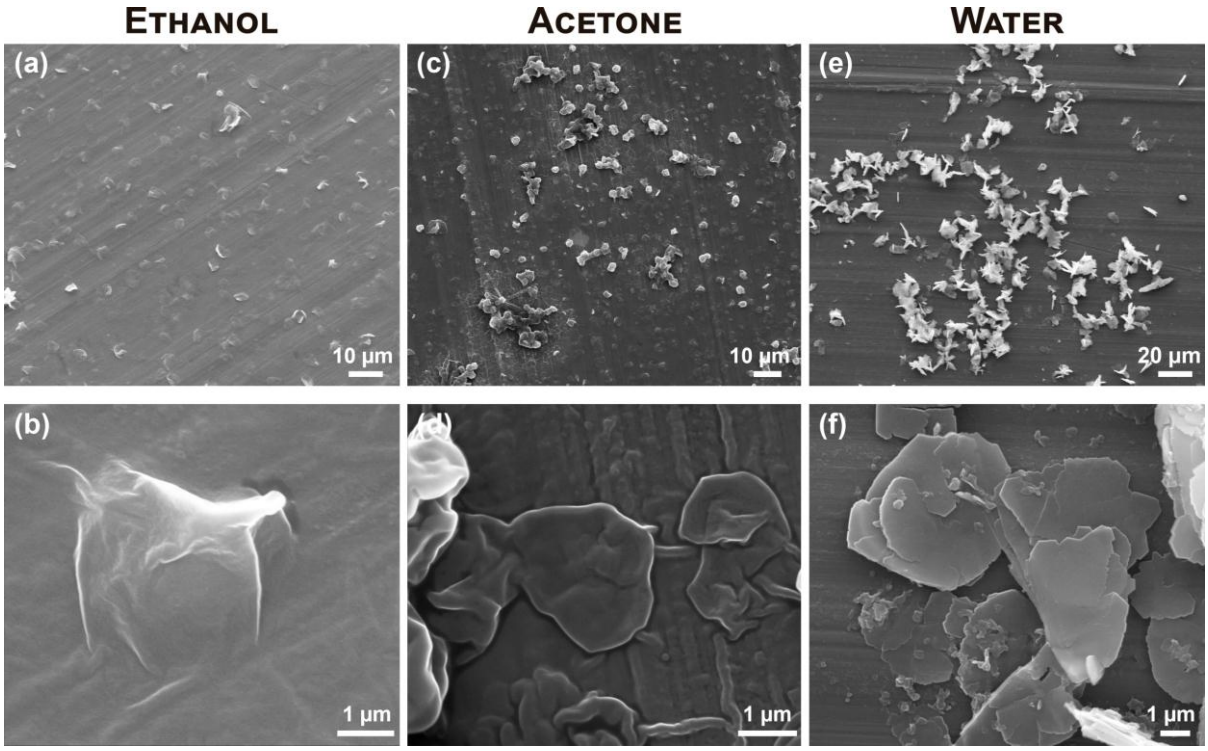

Figure 6. SEM images of the colloidal suspensions of complex **1** obtained after optimization of the sonication time with the probe tip and centrifugation (1 min, 7000 rpm) in (a-b) ethanol, (c-d) acetone and (e-f) water. Images (b), (d) and (f) are a large magnification images of the samples imaged in (a), (c) and (e) respectively. Images (a-d) prove the obtaining of films with lateral sizes of the order of 1-2 μm in ethanol and acetone. On the other hand, images (e-f) show the exfoliation of **1** into nanometre-thin films with lateral sizes of the order of 5 μm.

The delamination of complex **2** was also attempted sonicating with a probe tip for 20 minutes (see Supporting Information, Figure S22). Similar results to those previously obtained with ultrasound bath are found, mainly fragmentation of the crystals in ethanol and water and the obtaining of some flakes in acetone mixed with fragmented crystals. Different efforts to isolate the flakes from the larger crystalline aggregates by centrifugation or the use of different solvent combinations were unfruitful. The use of longer sonication time does not seem to be a solution, making evident the importance of chemical stability during the exfoliation process in order to achieve sufficient delamination yields for its isolation and consequent study (see Supporting Information Figure S23).

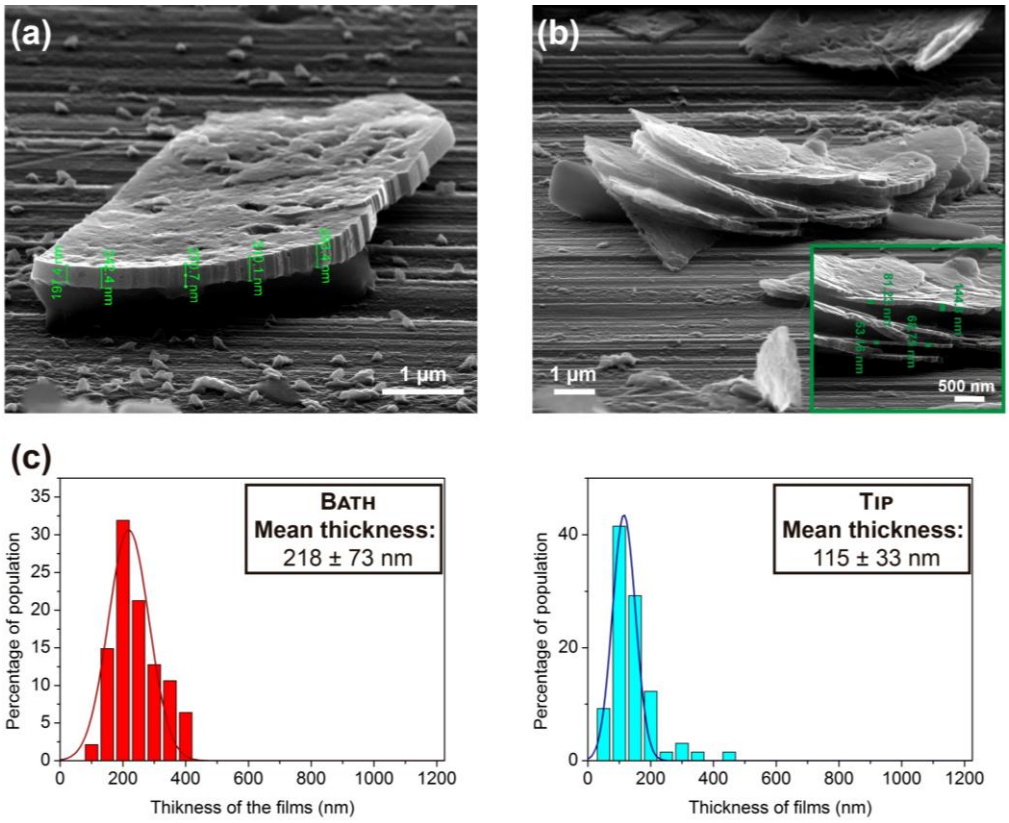

Figure 7. SEM cross section images of the colloidal suspensions of **1** in water obtained after optimization of the sonication time with (a) the ultrasound bath and (b) the probe tip and centrifugation for one minute at 7000 rpm. Some measurements on the thickness can be seen in green on the image (a) and the inset of image (b). (c) Size distributions of the thicknesses of films of complex **1** obtained with the optimized LPE process in water with the ultrasound bath (left) and with the probe tip (right).

Conclusion

Two novel cadmium-based 2D coordination polymers have been synthesized and characterized. The structure of $[Cd(oba)(bpfb)]_n \cdot xDMF$ (**1**), showed Cd(II) dimers coordinated by the dicarboxylic related ligands which occupy equatorial positions as chelate or bridging ligands; the axial positions were occupied by bpfb ligands which coordinate and strongly interconnect the Cd(II) dimers, forming a 2D layer. Voids between layers were occupied by DMF solvent molecules mostly stabilized through hydrogen bonds and weak VdW interactions. The structure of complex $[Cd(5\text{-aip})(DMF)_2]_n$, (**2**) showed the presence of Cd(II) dimers coordinated by the dicarboxylic ligands at the equatorial positions, both as chelate or bridging

ligands, resulting in the formation of a 2D layer; the axial positions were occupied by DMF molecules. Additionally, the solvent molecules of different 2D structures reinforce the structure by mean of numerous interactions between them. In this situation large energies are needed to break these interactions and replace these molecules with the assistant solvent and propitiate the delamination processes by reducing the cohesive forces between 2D layers.

Such differential role of the solvent molecules is claimed here as the origin of the different delamination behavior between both complexes. Indeed, while complex **1** can be delaminated, complex **2** failed in all the cases yielding a fragmented crystalline material from where it was impossible to isolate the flakes. We cannot discard the contribution of other factors. While complex **2** presents a unique ligand species and the 2D layer is built as a flat and non-highly compact structure, in complex **1** the 2D layers contains the intersection of two types of ligand-to-metal coordination: i) the coordination of the bpfb ligands to the Cd ions generating parallel double chains with strong interactions by π-π stacking forces, and ii) the coordination of the oba ligands as bridge ligands between Cd dimers which interconnect perpendicularly the double chains defined by the Cd dimers and bpfb ligands. In this disposition, oba ligands act as clamps that afford an extremely high stabilization of the 2D layer.

Delamination of complex **1** was achieved in water without the need of any external added energy whereas in the extreme situation delamination in DMF was not achieved even in the presence of additional ultrasound energy. This fact has been attributed to the interstitial DMF solvent molecules that remain within the voids generated in between layers stabilizing the structure. In between we can find solvents such as ethanol or acetone, which need the presence of additional ultrasound energy to induce the delamination, either ultrasound or tip-induced. These results confirm the role of the solvent in the delamination process.

Finally, a comparison of the delamination process done with an ultrasound bath or a tip was done. Both methods give rise to exfoliated flakes of similar characteristics. However, LPE with the ultrasound bath seemed to provide larger yields of exfoliation although longer sonication times are required. This hypothesis was supported by the observed pellets of non-exfoliated crystals after centrifuge, since they were larger in the suspensions obtained with the probe tip. Moreover, the flake morphology proved to be independent of the sonication power, being more relevant the nature of the solvent.

Materials and Methods

Chemicals and materials.

Cadmium nitrate tetrahydrate salt, 5-aminoisophtalic acid ligand (5-aip) and 4,4'-oxybis(benzoic acid) ligand (oba) were purchased in Sigma Aldrich.

Synthesis

Synthesis of complex μ-N,N'-bis(4-pyridyl formamide)-1,4-benzene (bpfb) ligand. bpfb ligand was synthesized by dissolving of p−phenylenediamine (1.081 mg, 10 mmol) in tetrahydrofuran (50 ml) and triethylamine (5.2 ml). Then, isonicotinic acid chloride was added. The overall was refluxed under stirring for 24 h. After cooling to room temperature, the yellow residue was filtered and was washed several times with sodium bicarbonate.

*Synthesis of complex **1***. The ligands bpfb (105 mg, 0.1 mmol) and oba (10.8 mg, 0.1 mmol) were dissolved in 15 ml DMF solvent and stirred 30 min, at room temperature. A solution of $Cd(NO_3)_2 \cdot 4H_2O$ (30.8 mg, 0.1 mmol) was added to the above-mentioned solution. The reaction mixture was placed in a Parr-Teflon lined stainless steel vessel. It was sealed and heated to 120°C for 2 days. The reaction mixture was cooled by slow cooling to the room temperature. Crystals of **1** were collected from the final reaction mixture by filtration and were air dried at ambient temperature. FT-IR (ATR mode, cm^{-1}): 3368 (w), 3051 (w), 1652 (s), 1594 (s), 1543 (s), 1513 (s), 1385 (s), 1318 (w), 1245 (s), 1159 (m), 1095 (m), 1066 (m), 1013 (m), 833 (m), 783 (s), 658 (s), 525 (s). Elemental analysis calculated for $[C32H22CdN4O7] \cdot 0.5DMF \cdot 2.95\ H_2O$: C, 51.8%; H, 4.09%; N, 8.15%. Found: C, 51.7%; H, 3.69%; N, 8.34%.

*Synthesis of complex **2***. 5-aminoisophthalic acid (5-aip) (18.07 mg, 0.1 mmol) and NaOH (8 mg, 0.2 mmol) were dissolved in 15 ml DMF and stirred 30 min, at room temperature. A solution of $Cd(NO_3)_2 \cdot 4H_2O$ (61.6 mg, 0.2 mmol) was added to the above-mentioned solution. The reaction mixture was placed in a Parr-Teflon lined stainless steel vessel. It was sealed and heated to 110°C for 2 days. The reaction mixture was cooled by slow cooling to the room temperature. Crystals of **2** were collected from the final reaction mixture by filtration and were air dried at the ambient temperature. FT-IR (ATR mode, cm^{-1}): 3330 (w), 3131 (w), 1608 (m), 1538 (s), 1368 (s), 1311 (s), 1039 (w), 968 (m), 814 (s), 774 (s), 735 (s), 579 (w).

Crystal cleaning and resuspension.

Crystals of complex **1** were cleaned and resuspended before the delamination process. The cleaning was performed dispersing the crystals in the same solvent used for their synthesis (DMF). The dispersions were subjected to three cycles of centrifugation at 6000 rpm for one minute. Centrifugation was performed with Sorvall Legend Micro 17R centrifuge (Thermo Scientific). Between cycles, the excess of DMF solvent was removed and replaced. The analyzed crystals were selected for delamination.

Hirshfeld surface analysis.

Molecular Hirshfeld surfaces have been constructed from CIF file, so that you can dissect crystal structures into noncovalent contacts.The very high-resolution Hirshfeld surfaces were generated by Crystal Explorer and functions of curvature, distance including shape index and d_{norm} were mapped to the surfaces. The normalized contact distance (d_{norm}) based on both d_e (distance from a point on the Hirshfeld surface to the nearest external nucleus) and d_i (distance from a point on the Hirshfeld surface to the nearest internal nucleus), and the vdW radii of the atom (r_i^{vdW} and r_e^{vdW}) , given by the following equation, enables identification of the regions of particular importance to intermolecular interactions: $d_{norm}= [(d_i – r_i^{vdW}) / r_i^{vdW}]+[(d_e – r_e^{vdW}) / r_e^{vdW}]$. The value of the d_{norm} is negative or positive when intermolecular contacts are shorter or longer than vdW separations, respectively. The combination of the distances from the Hirshfeld surface to the nearest nucleus inside the surface (d_i) and outside the surface (d_e) and the data conveyed by the shape index are consistent with 2D fingerprint plots. The 2D fingerprint maps of **1** and **2** provide some quantitative information gives the possibility of obtaining additional insight to the intermolecular interactions in the crystal state and for describing the surface characteristics of the molecules.

Liquid phase exfoliation.

Delamination was performed with the LPE method assisted by ultrasound. Two different set ups were investigated with different ultrasound generators: an ultrasound bath and a probe tip. Exfoliation parameters like sonication time and used solvent were optimized for both ultrasound sources.

Delamination with ultrasound bath. For this method, 0.5 to 1 mg of crystals were dispersed in 4 mL of four different solvents: DMF, ethanol, acetone and water. The dispersions were sonicated with ultrasound bath equipment (Elma S40H Elmasonic) kept at room temperature in order to avoid thermal decomposition of the complex. This equipment has an effective ultrasonic power of 140 W. Aliquots from every suspension were taken after 4, 6 and 8 hours of sonication.

Delamination with probe tip. In this case, 0.5 to 1 mg of crystals were dispersed in 4 mL of three different solvents: ethanol, acetone and water. Ultrasounds were applied with a Branson Digital Sonifier SFX 550 (Emerson) sonicator equipped with a double step 1/8 inch microtip. This equipment has an effective ultrasonic power of 550 W. The microtip was immersed in the dispersions to produce the assistant ultrasound. The dispersions also were stirred to avoid sedimentation of the crystals and were kept at room temperature in a water-ice bath in order to avoid thermal decomposition. Ultrasounds were applied in cycles of 2 minutes spaced by 30 seconds at 25% amplitude of the tip. Aliquots from every suspension were taken after 20, 40 and 80 minutes of sonication.

Isolation of 2D flakes.

Non-exfoliated bulk crystals in suspension after LPE process were removed by centrifugation. The flakes were remaining suspended in the supernatant. Aliquots from the suspensions were centrifuged for one minute at 7000 rpm. After delamination and centrifugation, the colloidal suspensions are kept under constant agitation in IKA HS 260 basic shaker. The complete exfoliation process was repeated with all the optimized parameters for full characterization of the obtained flakes.

Physico-chemical characterization of crystals.

Optical images were obtained with a Zeiss Primo Star microscope equipped with a Zeiss Axiocam ERc 5s camera on top. The software used for image acquirement was Zen Imaging Software (version ZEN 2012 blue edition). The crystals were dispersed on top of glassy and transparent microscope slides and put underneath the microscope. Powder X-ray diffraction (PXRD) patterns of the crystals were obtained with X'Pert3 Powder equipment (PANalytical), using Cu-Kα radiation. Intensity data were collected in continous-scan mode with a step size

of 0.0334° and time per step of 160.02 s (speed 0.026526°/s). Data from the equipment was recorded and treated with X'Pert Data collector software (PANalytical). The obtained patterns were compared to the one from the resolved structure with single crystal X-ray diffraction (SXRD). SXRD of **1** was carried out using a Rigaku XtaLAB Pro: Kappa single diffractometer delivering a Mo microfocus radiation (λMo K_α 0.71075 Å) and equipped with a HPAD PILATUS3 R 200K detector. SXRD of **2** was carried out at 120 K on a Supernova Agilent Technologies diffractometer equipped with a graphite-monochromated Enhance (Mo) X-ray Source (λ = 0.71073 Å). Suitable single crystal **2** was mounted on a glass fiber using a viscous hydrocarbon oil and then transferred directly to the cold nitrogen stream for data collection. The program CrysAlisPro, Agilent Technologies Ltd., was used for unit cell determinations and data reduction. Empirical absorption correction was performed using spherical harmonics, implemented in the SCALE3 ABSPACK scaling algorithm. Crystal structures were solved with direct methods with the SIR97 program, and refined against all F2 values with the SHELXL-2014 program, using the WinGX graphical user interface. All non-hydrogen atoms were refined anisotropically, and hydrogen atoms were placed in calculated positions and refined isotropically with a riding model. Fourier transform infrared spectroscopy (FT-IR) for both complexes was performed with Tensor 27 FT-IR spectrometer (Bruker) in attenuated total reflectance (ATR) mode. The instrument is equipped with a room temperature detector and a mid-IR source (4000 to 400 cm^{-1}). ATR was performed with a single window reflection of diamond model MKII Golden Gate, Specac. The spectra were recorded and treated with OPUS (Bruker) data collection software. Background spectrum in air was performed before the measurements, since the instrument is single beam. The dried samples were placed on the window reflection for measurement.

Physico-chemical characterization of flakes.

Flakes were characterized by Scanning Electron Microscopy (SEM) with SEM FEI Quanta 650F microscope. The samples were prepared by drop-casting of the aliquots onto metallic sample holders. After evaporation of the solvent under ambient conditions, the previously suspended flakes remained on the holders. A 5 nm Pt layer was sputtered with Leica EM ACE600 on top of the samples, reproducing their topography. Afterwards, the particles were imaged with high acceleration voltages, between 10 to 20 kV at a working distance of 10 mm.

Cross –section images were taken tilting the sample 70°. Stability of the colloidal suspension was characterized by Dynamic Light Scattering (DLS) with Zetasizer Nano 3600 equipment (Malvern Instruments, UK) at 25°C. The data was collected with Zetasizer 7.02 software. Measurements were performed by introducing 1 mL of sample in disposable plastic cuvettes. FT-IR of the flakes was performed with Hyperion 2000 FT-IR microscope (Bruker) working in reflection mode. The instrument is equipped with a room temperature detector and a mid-IR source (4000 to 600 cm^{-1}). The spectra were recorded and treated with OPUS data collection software. Samples were prepared by drop-casting of the colloidal suspensions on top of gold substrates and left evaporated under ambient conditions.

Acknowledgements

This work was supported by grant MAT 2015-70615-R from the Spanish Government funds and by the European Regional Development Fund (ERDF). Funded by the CERCA Program/Generalitat de Catalunya, ICN2 is supported by the Severo Ochoa program from Spanish Ministry of Economy, Industry and Competitiveness (MINECO) (Grant No. SEV-2017-0706). Noemí Contreras-Pereda has received financial support through the “la Caixa” Fellowship Grant for Doctoral Studies, “la Caixa” Banking Foundation, Barcelona, Spain. Salvio Suárez-García acknowledges the support from MINECO BES-2015-071492 grant. Samia Benmansour thanks the Generalitat Valenciana (Prometeo2014/II/076 project) and the Spanish MINECO (Project CTQ2017-87201-P AEI/FEDER, EU) for financial support.

Keywords: 2D-structures, coordination polymers, nanomaterials, delamination process, ultrasound-assisted process

[1] A.K. Geim, I.V. Grigorieva, Van der Waals heterostructures, *Nature* 499 (**2014**) 419-425. https://doi.org/10.1038/nature12385.

[2] R. Mas-Ballesté, C. Gómez-Navarro, J. Gómez-Herrero, F. Zamora, 2D materials: to graphene and beyond, *Nanoscale* 3 (**2011**) 20-30. https://doi.org/10.1039/C0NR00323A.

[3] (a) J. Kang, H. Kim, K.S. Kim, S.K. Lee, S. Bae, J.H. Ahn, Y.J Kim, J.B. Choi, B.H. Hong, High-Performance Graphene-Based Transparent Flexible Heaters, *Nano Lett.* 11 (**2011**) 5154-5158. https://dx.doi.org/10.1021/nl202311v. (b) Y.-M. Lin, C. Dimitrakopoulos, K.A. Jenkins, D.B. Farmer, H.Y. Chiu, A. Grill, P. Avouris, 100-GHz Transistors from Wafer-Scale Epitaxial Graphene, *Science* 327 (**2010**) 662-662. https://dx.doi.org/10.1126/science.1184289. (c) Y. Wu, Y.M. Lin, A.A. Bol, K.A. Jenkins, F. Xia, D.B Farmer, Y. Zhu, P. Avouris, High-frequency, scaled graphene transistors on diamond-like carbon, *Nature* 472 (**2011**) 74-78. https://doi.org/10.1038/nature09979. (d) F.K. Perkins, A.L. Friedman, E. Cobas, P.M. Campbell, G.G. Jernigan, B.T. Jonker, Chemical Vapor Sensing with Monolayer MoS2, *Nano Lett.* 13 (**2013**) 668-673. https://dx.doi.org/10.1021/nl3043079. (e) Vu, Q. A., Shin, Y.S., Kim, Y.R., Kang, W.T., Kim, H., Luong, D.H., Lee, I.M., Lee, K., Ko, D.S., Heo, J., Park, S., Lee, Y.H., Yu, W.J., 2018. Two-terminal floating-gate memory with van der Waals heterostructures for ultrahigh on/off ratio. *Nat. Commun*. 7, 12725. https://doi.org/10.1038/ncomms12725.

[4] (a) D.J. Ashworth, J.A. Foster, Metal-organic framework nanosheets (MONs): a new dimension in materials chemistry, *J. Mater. Chem. A* 6 (**2018**) 16292-16307. https://doi.org/10.1039/c8ta03159b. (b) M. Zhao, Y. Huang, Y. Peng, Z. Huang, Q. Ma, H. Zhang, Two-dimensional metal–organic framework nanosheets: synthesis and applications, *Chem. Soc. Rev*. 47 (**2018**), 6267-6295. https://doi.org/10.1039/c8cs00268a. (c) Furukawa, H., Cordova, K.E., Yaghi, O.M., 2013. The Chemistry and Applications of Metal-Organic Frameworks. *Science* 3, 1230444. https://doi.org/10.1126/science.1230444.

[5] Y. Wang, M. Zhao, J. Ping, B. Chen, X. Cao, Y. Huang, C. Tan, Q. Ma, S. Wu, Y. Yu, Q. Lu, J. Chen, W. Zhao, Y. Ying, H. Zhang, Bioinspired Design of Ultrathin 2D Bimetallic Metal-Organic-Framework Nanosheets Used as Biomimetic Enzymes, *Adv. Mater.* 28 (**2016**) 4149-4155. https://doi.org/10.1002/adma.201600108.

[6] G. Xu, T. Yamada, K. Otsubo, S. Sakaida, H. Kitagawa, Facile “modular assembly” for fast construction of a highly oriented crystalline MOF nanofilm, *J. Am. Chem. Soc.* 134 (**2012**) 16524-16527. https://doi.org/10.1021/ja307953m.

[7] Y. Peng, Y. Li, Y. Ban, H. Jin, W. Jiao, X. Liu , W. Yang, Metal-organic framework nanosheets as building blocks for molecular sieving membranes, *Science* 346 (**2014**) 1356-1359. https://doi.org/10.1126/science.1254227.

[8] Y. Zhang, X. Feng, S. Yuan, J. Zhou, B. Wang, Challenges and recent advances in MOF-polymer composite membranes for gas separation, *Inorg. Chem. Front.* 3 (**2016**) 896-909. https://doi.org/10.1039/C6QI00042H.

[9] H.B.T. Jeazet, C. Staudt, C. Janiak, Metal-organic frameworks in mixed-matrix membranes for gas separation, *Dalton Trans.* 41 (**2012**) 14003-14027. https://doi.org/10.1039/C2DT31550E.

[10] G. Zhan, H.C. Zeng, An alternative synthetic approach for macro-meso-microporous metal-organic frameworks via a “domain growth” mechanism, *Chem. Commun.* 52 (**2016**) 8432-8435. https://doi.org/10.1039/C6CC03555H.

[11] R. Dong, M. Pfeffermann, H. Liang, Z. Zheng, X. Zhu, J. Zhang, X. Feng, Large-Area, Free-Standing, Two-Dimensional Supramolecular Polymer Single-Layer Sheets for Highly Efficient Electrocatalytic Hydrogen Evolution, *Angew. Chem. Int. Edit.* 54 (**2015**) 12058-12063. https://doi.org/10.1002/anie.201506048.

[12] C. Hermosa, B.R. Horrocks, J.I. Martinez, F. Liscio, J. Gomez-Herrero, F. Zamora, Mechanical and optical properties of ultralarge flakes of a metal-organic framework with molecular thickness, *Chem. Sci.* 6 (**2015**) 2553-2558. https://doi.org/10.1039/C4SC03115F.

[13] T. Araki, A. Kondo, K. Maeda, The first lanthanide organophosphonate nanosheet by exfoliation of layered compounds, *Chem. Commun.* 49 (**2013**) 552-554. https://doi.org/10.1039/C2CC36703C.

[14] W. Zhao, J. Peng, W. Wang, S. Liu, Q. Zhao, W. Huang, Ultrathin two-dimensional metal-organic framework nanosheets for functional electronic devices, *Coordin. Chem. Rev.* 377 (**2018**) 44-63. https://doi.org/10.1016/j.ccr.2018.08.023.

[15] G. Wu, J. Huang, Y. Zang, J. He, G. Xu, Porous field-effect transistors based on a semiconductive metal-organic framework, *J. Am. Chem. Soc.* 139 (**2017**) 1360-1363. https://doi.org/10.1021/jacs.6b08511.

[16] M.S. Yao, X.J. Lv, Z.H. Fu, W.H. Li, W.H. Deng, G.D. Wu, G. Xu, Layer-by-Layer Assembled Conductive Metal-Organic Framework Nanofilms for Room-Temperature Chemiresistive Sensing*, Angew. Chem. Int. Edit.* 56 (**2017**) 16510-16514. https://doi.org/10.1002/anie.201709558.

[17] M.K. Smith, K.A. Mirica, Self-Organized Frameworks on Textiles (SOFT): Conductive Fabrics for Simultaneous Sensing, Capture, and Filtration of Gases, *J. Am. Chem. Soc.* 139 (**2017**) 16759-16767. https://doi.org/10.1021/jacs.7b08840.

[18] Miner, E.M., Fukushima, T., Sheberla, D., Sun, L., Surendranath, Y., Dincă, M., 2016. Electrochemical oxygen reduction catalysed by Ni3(hexaiminotriphenylene)2, *Nat. Commun*. 7, 10942. https://doi.org/10.1038/ncomms10942.

[19] D. Sheberla, J.C Bachman., J.S. Elias, C.J. Sun, Y. Shao-Horn, M. Dincă, Conductive MOF electrodes for stable supercapacitors with high areal capacitance, *Nat. Mater.*16 (**2017**) 220-224. https://doi.org/10.1038/nmat4766.

[20] Li, W. H., Ding, K., Tian, H.R., Yao, M.S., Nath, B., Deng W.H., Wang, Y., Xu, G., 2017. Conductive Metal-Organic Framework Nanowire Array Electrodes for High-Performance Solid-State Supercapacitors. *Adv. Funct. Mater.* 27, 1702067. https://doi.org/10.1002/adfm.201702067.

[21] D. Feng, T. Lei, M.R. Lukatskaya, J. Park, Z. Huang, M. Lee, L. Shaw, S. Chen, A.A. Yakovenko, A. Kulkarni, J. Xiao, K. Fredrickson, J.B. Tok, X. Zou, Y. Cui, Z. Bao, Robust and conductive two-dimensional metal-organic frameworks with exceptionally high volumetric and areal capacitance, *Nat. Energy* 3 (**2018**) 30-36. https://doi.org/10.1038/s41560-017-0044-5.

[22] S. Suárez-García, N.N. Adarsh, G. Molnar, A. Bousseksou, Y. García, M.M. Dirtû, J. Saiz-Poseu, R. Robles, P. Ordejón, D. Ruiz-Molina, Spin-Crossover in an Exfoliated 2D Coordination Polymer and Its Implementation in Thermochromic Films *ACS Appl. Nano Mater.* 1 (**2018**) 2662-2668. https://doi.org/10.1021/acsanm.8b00341.

[23] J. Liu, H. Yu, L. Wang, Z. Deng, K. Naveed, A. Nazir, F. Haq, Two-dimensional metal-organic frameworks nanosheets: Synthesis strategies and applications, *Inorg. Chim. Acta* 483 (**2018**) 550-564. https://doi.org/10.1016/j.ica.2018.09.011.

[24] L. Cao, T. Wang, C. Wang, Synthetic Strategies for Constructing Two-Dimensional Metal-Organic Layers (MOLs): A Tutorial Review, *Chin. J. Chem.* 36 (**2018**) 754-764. https://doi.org/10.1002/cjoc.201800144.

[25] R. Sakamoto, K. Takada, X. Sun, T. Pal, T. Tsukamoto, E.J.H. Phua, A. Rapakousiou, K. Hoshiko, H. Nishihara, The coordination nanosheet (CONASH), *Coordin. Chem. Rev.* 320-321 (**2016**) 118-128. https://doi.org/10.1016/j.ccr.2015.12.001.

[26] T. Rodenas, I. Luz, G. Prieto, B. Seoane, H. Miro, A. Corma, F. Kapteijn, F.X. Llabrés i Xamena, J. Gascón, Metal-organic framework nanosheets in polymer composite materials for gas separation, *Nat. Mater.*14 (**2015**) 48-55. https://doi.org/10.1038/nmat4113.

[27] A. Sengupta, S. Datta, C. Su, T.S. Herng, J. Ding, J.J. Vittal, K.P. Loh, Tunable Electrical Conductivity and Magnetic Property of the Two Dimensional Metal Organic Framework [Cu(TPyP)Cu2(O2CCH3)4], *ACS Appl. Mater. Interfaces* 8 (**2016**) 16154-16159. https://doi.org/10.1021/acsami.6b03073.

[28] M. Shete, P. Kumar, J.E. Bachman, X. Ma, Z.P. Smith, W. Xu, K.A. Mkhoyan, J.R. Long, M. Tsapatsis, On the direct synthesis of Cu(BDC) MOF nanosheets and their performance in mixed matrix membranes, *J. Membrane Sci.* 549 (**2018**) 312-320. https://doi.org/10.1016/j.memsci.2017.12.002.

[29] He, T., Ni, B., Zhang, S., Gong, Y., Wang, H., Gu, L., Zhuang, J., Hu, W., Wang, X., 2018. Ultrathin 2D Zirconium Metal-Organic Framework Nanosheets: Preparation and Application in Photocatalysis. *Small*. 14, 1703929. https://doi.org/10.1002/smll.201703929.

[30] F. Xue, P. Kumar, W. Xu, K.A. Mkhoyan, M. Tsapatsis, Direct Synthesis of 7 nm-Thick Zinc(II)-Benzimidazole-Acetate Metal-Organic Framework Nanosheets, *Chem. Mater.* 30 (**2018**) 69-73. https://doi.org/10.1021/acs.chemmater.7b04083.

[31] K. Zhao, S. Liu, G. Ye, Q. Gan, Z. Zhou, Z. He, High-yield bottom-up synthesis of 2D metal-organic frameworks and their derived ultrathin carbon nanosheets for energy storage, *J. Mater. Chem. A* 6 (**2018**) 2166-2175. https://doi.org/10.1039/C7TA06916B.

[32] S.C. Junggeburth, L. Diehl, S. Werner, V. Duppel, W. Sigle, B.V. Lotsch, Ultrathin 2D Coordination Polymer Nanosheets by Surfactant-Mediated Synthesis, *J. Am. Chem. Soc.* 135 (**2013**) 6157-6164. https://doi.org/10.1021/ja312567v.

[33] J.A. Foster, S. Henke, A. Schneemann, R.A. Fischer, A.K. Cheetham, Liquid exfoliation of alkyl-ether functionalised layered metal-organic frameworks to nanosheets, *Chem. Commun.* 52 (**2016**)10474-10477. https://doi.org/10.1039/C6CC05154E.

[34] P.Z. Li, Y. Maeda, Q. Xu, Top-down fabrication of crystalline metal-organic framework nanosheets, *Chem. Commun.* 47 (**2011**) 8436-8438. https://doi.org/10.1039/C1CC12510A.

[35] P. Amo-Ochoa, L. Welte, R. González-Prieto, P.J.S. Miguel, C.J. Gómez-García, E. Mateo-Martí, S. Delgado, J. Gómez-Herrero, F. Zamora, Single layers of a multifunctional laminar Cu(I,II) coordination polymer, *Chem. Commun.* 46 (**2010**) 3262-3264. https://doi.org/10.1039/B919647A.

[36] H. Xu, J. Gao, X. Qian, J. Wang, H. He, Y. Cui, Y. Yang, Z. Wang, G. Qian, Metal-organic framework nanosheets for fast-response and highly sensitive luminescent sensing of Fe3+, *J. Mater. Chem. A* 4 (**2016**) 10900-10905. https://doi.org/10.1039/C6TA03065C.

[37] A. Gallego, C. Hermosa, O. Castillo, I. Berlanga, C.J. Gómez-García, E. Mateo-Martí, J.I. Martínez, F. Flores, C. Gómez-Navarro, J. Gómez-Herrero, S. Delgado, F. Zamora, Solvent-Induced Delamination of a Multifunctional Two Dimensional Coordination Polymer, *Adv. Mater.* 25 (**2013**) 2141-2146. https://doi.org/10.1002/adma.201204676.

[38] S. Benmansour, A. Abhervé, P. Gómez-Claramunt, C. Vallés-García, C.J. Gómez-García, Nanosheets of Two-Dimensional Magnetic and Conducting Fe(II)/Fe(III) Mixed-Valence Metal-Organic Frameworks. *ACS Appl. Mater. Interfaces* 9 (**2017**) 26210–26218. https://doi.org/10.1021/acsami.7b08322.

[39] Han, L.J., Zheng, D., Chen, S.G., Zheng, H.G., Ma, J., 2018. A Highly Solvent-Stable Metal-Organic Framework Nanosheet: Morphology Control, Exfoliation, and Luminescent Property. *Small*. 14, 1703873. https://doi.org/10.1002/smll.201703873.

[40] C. Kutzscher, A. Gelbert, S.Ehrling, C. Schenk, I. Senkovska, S. Kaskel, Amine assisted top-down delamination of the two-dimensional metal-organic framework Cu2(bdc)2, *Dalton Trans.* 46 (**2017**) 16480-16484. https://doi.org/10.1039/C7DT03890A.

[41] Y. Ding, Y.P. Chen, X. Zhang, L. Chen, Z. Dong, H.L. Jiang, H. Xu, H.C. Zhou, Controlled Intercalation and Chemical Exfoliation of Layered Metal-Organic Frameworks Using a

Chemically Labile Intercalating Agent, *J. Am. Chem. Soc.* 139 (**2017**) 9136-9139. https://doi.org/10.1021/jacs.7b04829.

[42] S. Goswami, L. Ma, A.B.F. Martinson, M.R. Wasielewski, O.K. Farha, J.T. Hupp, Toward Metal-Organic Framework-Based Solar Cells: Enhancing Directional Exciton Transport by Collapsing Three-Dimensional Film Structures, *ACS Appl. Mater. Interfaces* 8 (**2016**) 30863-30870. https://doi.org/10.1021/acsami.6b08552.

[43] B. Garai, A. Mallick, A. Das, R. Mukherjee, R. Banerjee, Self-Exfoliated Metal-Organic Nanosheets through Hydrolytic Unfolding of Metal-Organic Polyhedra, *Chem.-Eur. J.* 23 (**2017**) 7361-7366. https://doi.org/10.1002/chem.201700848.

[44] H.S. Quah, L.T. Ng, B. Donnadieu, G.K. Tan, J.J. Vittal, Molecular Scissoring: Facile 3D to 2D Conversion of Lanthanide Metal Organic Frameworks Via Solvent Exfoliation, *Inorg. Chem.* 55 (**2016**) 10851-10854. https://doi.org/10.1021/acs.inorgchem.6b02222.

[45] G. Das, B.P. Biswal, S. Kandambeth, V. Venkatesh, G. Kaur, M. Addicoat, T. Heine, S. Verma, R. Banerjee, Chemical sensing in two dimensional porous covalent organic nanosheets, *Chem. Sci.* 6 (**2015**) 3931-3939. https://doi.org/10.1039/C5SC00512D.